

DESIGN AND PERFORMANCE OF HIGH LASER POWER INTERFEROMETERS FOR
GRAVITATIONAL-WAVE DETECTION

By

KATHERINE L DOOLEY

A DISSERTATION PRESENTED TO THE GRADUATE SCHOOL
OF THE UNIVERSITY OF FLORIDA IN PARTIAL FULFILLMENT
OF THE REQUIREMENTS FOR THE DEGREE OF
DOCTOR OF PHILOSOPHY

UNIVERSITY OF FLORIDA

2011

© 2011 Katherine L Dooley

For Grandmom

ACKNOWLEDGMENTS

Some personal acknowledgements—professors, fellow grad students, friends, family.

Acknowledgments for the funding of LIGO.

This work was supported by the US National Science Foundation grants PHY-xxxxxxx and PHY-xxxxxxx to the University of Florida, Gainesville, Florida.

And David Feldbaum says I must include a thank you for him because I made him search the elog for a spiricon BCS picture one too many times for me.

My neighbor Noah Goldfish for introducing me to Andri Gretarsson who in turn recommended me to the UF group. Guido and Dave for following through with recruiting me despite the fact I had already accepted grad school admission elsewhere! (well outside of the established grad school admissions timeline), and for supporting my desire to reside at the site.

TABLE OF CONTENTS

	<u>page</u>
ACKNOWLEDGMENTS	4
LIST OF TABLES	7
LIST OF FIGURES	8
LIST OF SYMBOLS	10
ABSTRACT	11
CHAPTER	
1 Purpose of this work	12
2 The Search for Gravitational Waves	13
2.1 The theory of gravitational radiation	13
2.2 Sources	14
2.3 Methods of detection	15
2.4 State of ground-based interferometry	15
3 Laser interferometers for gravitational-wave detection	18
3.1 Signal versus noise	18
3.1.1 Displacement noise	18
3.1.2 Sensing noise	18
3.2 Power-recycled Fabry-Perot Michelson	19
3.3 Measuring GW strain with light	19
3.3.1 Light as a photon	19
3.3.2 Light as a wave	20
3.4 Power Recycled Michelson Interferometers	21
3.5 More Laser Power	21
3.6 Digital Control in LIGO	21
4 Angular mirror motion	22
4.1 Introduction	22
4.2 The mirrors as torsion pendula	22
4.2.1 Torque to angle transfer function	23
4.3 Seismic noise torque	25
4.4 Actuation noise torque	25
4.5 Radiation pressure torque	26
4.5.1 Tilt eigenmodes of a Fabry-Perot cavity	27
4.5.2 Soft and hard modes	29
4.5.3 Stability	31
4.6 How much suppression is necessary?	33

4.7	Appendix xx–misaligned cavity axis	33
5	Sensing and controlling mirror motion in the radiation pressure eigenbasis	36
5.1	Introduction	36
5.2	Sensing	36
5.2.1	OSEMs	36
5.2.2	Optical levers	36
5.2.3	Camera image	37
5.2.4	QPDs	38
5.2.5	WFSs	38
5.3	Control	38
5.4	Sensor noise and noise contribution to DARM	38
5.5	Solving the noise problem with the eigenbasis	38
5.6	ASC to DARM noisebudget	38
5.7	Beam spot motion	41
5.8	Heating related measurements	41
5.9	DC readout related measurements	41
5.10	ASC noisebudget	41
6	Experimental measurement of the Sidles-Sigg effect	43
6.1	Measured modes	43
7	Summary	44
	REFERENCES	46
	BIOGRAPHICAL SKETCH	48

LIST OF TABLES

<u>Table</u>	<u>page</u>
4-1 Geometric parameters of the LIGO arm cavity eigenmodes. x_i are the beam locations on the mirrors relative to center, a is the cavity axis displacement at the waist, and α is the cavity axis angle with respect to a line joining the centers of the mirrors. Differences between LLO and LHO arise from the mirrors having different radii of curvature at the two sites.	29
4-2 Torsional constants (pitch) for the soft and hard modes of a typical Initial LIGO power and the highest of Enhanced LIGO powers. The soft mode in Enhanced LIGO is unstable.	31
4-3 Conditions on torsional constant κ for determining system stability.	32

LIST OF FIGURES

<u>Figure</u>	<u>page</u>
2-1 Strain sensitivities of LIGO-VIRGO collaboration interferometers.	16
3-1 Power-recycled Fabry-Perot Michelson laser interferometer.	19
4-1 Cartoon of a LIGO suspension. Improve this.	23
4-2 Torque to pitch transfer function of a LIGO core optic (blue). The optic acts like a free mass at high frequencies (green) and the DC magnitude of the transfer function is determined by the inverse torsional constant (red). A damping constant $\gamma = 0.006$ ($Q = 32$) was selected for pictorial reasons only.	25
4-3 Typical angular motion of the core suspended mirrors in the absence of interferometric control. Velocity damping provided by the OSEMs and the optical levers is present. Above about 30 Hz, the plot does not represent real motion; the spectrum is limited by sensor (optical lever) noise. Show the quadrature sum of angular motion due to the three sources discussed in this section.	26
4-4 Angular motion induced by a 1% coupling of length actuation to angle.	26
4-5 Illustration of the orthogonal modes of cavity tilt. The upper diagram shows tilts given by eigenvector \vec{v}_2 and the lower diagram shows \vec{v}_1	29
4-6 Torsional spring constants (pitch) of an optically coupled cavity for LLO parameters. The soft mode is unstable when the spring constant is negative.	32
4-7 Single cavity opto-mechanical transfer function for pitch. The resonant frequency increases with power for the hard mode, but decreases for the soft mode, eventually becoming imaginary. $P_{circ} = 9$ kW (5.25 W input) was a typical operating power for Initial LIGO and $P_{circ} = 40$ kW (23.5 W input) is the highest of powers reached for Enhanced LIGO.	33
4-8 Torque to pitch transfer function (upper plot) and poles (lower plot) as a function of torsional constant for a fixed damping coefficient of $\gamma^2/4I = 1.77 \times 10^{-4}$. Circles show s_+ and dots show s_- . Poles in the right half of the s-plane indicate the system is unstable. This range of κ represents the torsional constants experienced while powering up Enhanced LIGO.	34
5-1 Image of beam on beam splitter as used for the beam centering servo.	37
5-2 Pitch open loop gains of the 5 WFS loops as measured with 6 W input power.	39
5-3 WFS sensor noise budget.	39

5-4	Top: Comparison of motion with and without the ASC. Eigenbasis residual during 10 W lock, and background derived from loop correction. Completely different day from bottom plot. Bottom: Propagation of sensor signals from 10 W lock through input matrix and power scaling to eigenbasis, compared with eigenbasis reconstruction of optical lever signals when interferometer not locked, but optics under oplev damping. Data are taken 45 minutes apart.	40
5-5	Effect of the WFS1 lowpass filter cutoff frequency on strain sensitivity.	41
7-1	Reflected beam from the Advanced LIGO pre-mode cleaner.	45

LIST OF SYMBOLS, NOMENCLATURE, AND ABBREVIATIONS

ASC	Angular Sensing and Control
EOM	electro-optic modulator
FI	Faraday isolator
GW	gravitational wave
IO	Input Optics
LIGO	Laser Interferometer Gravitational-wave Observatory
LSC	length sensing and control
MC	mode cleaner
MMT	mode matching telescope
PSL	pre-stabilized laser
PRC	power recycling cavity
REFL	reflected beam
RF	radio frequency
RM	recycling mirror
TGG	Terbium Gallium Garnate
TM	test mass
VIRGO	Variability of Solar Irradiance and Gravity Oscillations
WFS	wave-front sensor

Abstract of dissertation Presented to the Graduate School
of the University of Florida in Partial Fulfillment of the
Requirements for the Degree of Doctor of Philosophy

DESIGN AND PERFORMANCE OF HIGH LASER POWER INTERFEROMETERS FOR
GRAVITATIONAL-WAVE DETECTION

By

Katherine L Dooley

September 2011

Chair: David Reitze

Major: Physics

My abstract.

CHAPTER 1

PURPOSE OF THIS WORK

The purpose of this work is to demonstrate the capability of an interferometric gravitational wave detector to operate at several times the highest of laser powers previously used. From a naïve standpoint, more power is desirable since strain sensitivity improves by \sqrt{P} in the high frequency (> 200 Hz) shot-noise-limited region. However, as detectors become more sensitive at low frequencies (< 70 Hz), radiation pressure noise will become the dominant noise source, making high laser power operation a design trade-off. Currently, seismic noise limits low frequency sensitivity, so exploring the technical world of increasing the laser power is a fruitful adventure.

Operation of Initial LIGO was limited to 7 W input power due to uncontrolled radiation pressure torque instabilities in the arm cavities. Explained theoretically by Sidles and Sigg [1], measured experimentally by Hirose [2], and modeled numerically by Barsotti [3], the effect of radiation pressure torque on angular alignment needed to be addressed in practice in order for Enhanced LIGO to succeed in operating at powers greater than 7 W. We present the re-designed Angular Sensing and Control (ASC) system as implemented on the Enhanced LIGO detectors and show results of its performance with up to 20 W input power, demonstrating good agreement between theory, experiment and model.

The use of more power also complicates interferometer operations because of thermal effects. The optics which condition the laser for use in the interferometer experienced degradation in their performance in Initial LIGO as the result of absorbing too much heat. Less absorptive optical components were chosen with the goal of conquering thermal issues at the source, and changes were made to the architecture of the Input Optics to compensate for any residual effects. We present the re-designed Input Optics and their thermal performance with up to 30 W input power.

CHAPTER 2

THE SEARCH FOR GRAVITATIONAL WAVES

The field of ground-based gravitational-wave (GW) physics is rapidly approaching a state with a high likelihood of detecting GWs for the first time. Such a detection will not only validate part of Einstein's general theory of relativity, but initiate an era of astrophysical observation of the universe through GWs. Gravitational waves are dynamical strains in space-time that travel at the speed of light and are generated by non-axisymmetric acceleration of mass. The frequency of the gravitational wave depends on its source. A first detection is expected to witness an event such as a supernova or binary black hole/neutron star merger. This chapter provides the theoretical framework of gravitational wave generation and presents various ways to detect them, including the current status of an effort to do so.

2.1 The theory of gravitational radiation

Gravitational radiation is a perturbation $|h_{\mu\nu}| \ll 1$ to the flat space-time Minkowski metric $\eta_{\mu\nu} = \text{diag}(-1, 1, 1, 1)$. The metric describing space-time in the presence of gravitational radiation is therefore

$$g_{\mu\nu} = \eta_{\mu\nu} + h_{\mu\nu}. \quad (2.1.1)$$

Just as in electrodynamics where one has freedom in choosing the vector potential \vec{A} for calculating the magnetic field $\vec{B} = \vec{\nabla} \times \vec{A}$, one also has freedom in general relativity in choosing the form of $h_{\mu\nu}$ for ease of calculation. A convenient and popular choice is called the transverse-traceless (TT) gauge in which

$$h_{\mu\nu} = \begin{bmatrix} 0 & 0 & 0 & 0 \\ 0 & h_+ & h_\times & 0 \\ 0 & h_\times & -h_+ & 0 \\ 0 & 0 & 0 & 0 \end{bmatrix} \quad (2.1.2)$$

where the $+$ and \times represent two linearly independent polarizations. Without loss of generality, we consider the h_+ polarization in the example that follows.

For a gravitational wave traveling along the z axis, the metric is given by:

$$ds^2 = -c^2 dt^2 + [1 + h_+(t)]dx^2 + [1 - h_+(t)]dy^2. \quad (2.1.3)$$

This says the TT coordinate system is stretched along the x axis and compressed along the y axis by a factor of

$$\sqrt{1 \pm h_+(t)} \approx 1 \pm \frac{1}{2}h_+(t). \quad (2.1.4)$$

Therefore, the *proper distance* between two free masses located along either the x or the y axes changes by the factor in Eq. 2.1.4; their coordinate separations remain constant. The GW perturbation is a dimensionless strain

$$h = 2 \frac{\Delta L}{L}. \quad (2.1.5)$$

2.2 Sources

Any object with an accelerating mass quadrupole moment generates gravitational waves. The typical strain amplitudes, however, are extremely tiny: a binary system of coalescing $1M_\odot$ neutron stars in the Virgo Cluster (a distance of 15 Mpc) would produce a maximum GW strain on Earth of only 10^{-21} . The strain is proportional to source mass and velocity, and inversely proportional to distance from the observer:

$$h \approx \frac{GMv^2}{Rc^4} \quad (2.2.1)$$

Consequently, the most promising sources of detectable gravitational waves are nearby, fast-moving, massive astrophysical objects that include

- supernovae
- binary stars (orbiting or coalescing)
- spinning neutron stars
- cosmological/astrophysical background

and can be categorized as producing periodic, burst, or stochastic GWs.

Stably orbiting binary star systems comprised of black holes or neutron stars as well as rapidly spinning non-axisymmetric pulsars are considered periodic sources since they will

produce GWs of relatively constant frequency. These reliable sources of GWs require a long integration time to pick out their signal above noise. The Hulse-Taylor binary, for instance, falls into this category. Supernovae are burst sources since the gravitational collapse will produce a short-lived, unmodeled emission of GWs. Binaries in their final tens of milliseconds of inspiral also fall into this category. Finally, the anisotropies in the inflation of the universe together with the hum of all distant astrophysical sources will create a stochastic background of radiation. Coherent cross-correlation between multiple detectors is necessary for measuring the constant amplitude, broad-spectrum GW background.

Directly detecting gravitational radiation from any such source will reveal information that electromagnetic radiation cannot convey. The frequency of the GW tells about the dynamical timescale of the source. Only through GW radiation, for example, can mass and spin properties of a black hole be revealed.

2.3 Methods of detection

- Hulse/Taylor
- Resonant bars
- Pulsar timing
- CMB polarization (B-modes)
- Interferometry

For an approachable overview of the history of the field, including detector design choices and estimated GW strain amplitudes of various sources, refer to Ref. [4].

2.4 State of ground-based interferometry

A network of first generation kilometer scale laser interferometer gravitational-wave detectors completed its integrated 2-year data collection run in 2007, called S5. The instruments were: the American Laser Interferometer Gravitational-wave Observatories (LIGO)[5], one in Livingston, LA with 4 km long arms and two in Hanford, WA with 4 km and 2 km long arms; the 3 km French-Italian detector VIRGO[6] in Cascina, Italy; and the 1.2 km German-British

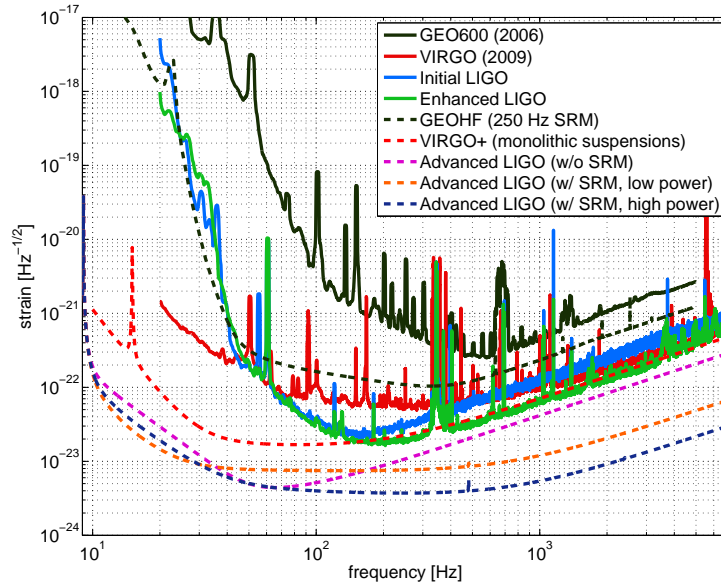


Figure 2-1. Strain sensitivities of LIGO-VIRGO collaboration interferometers.

detector GEO[7] in Ruthe, Germany. Multiple separated detectors increase detection confidence through signal coincidence and improve source localization through triangulation.

The first generation of LIGO, known as Initial LIGO, achieved its design goal of sensitivity to GWs in the 40 Hz - 7000 Hz band which included an impressive record strain sensitivity of $2 \times 10^{-23} / \sqrt{\text{Hz}}$ at 155 Hz. However, only the loudest of sources produce enough GW strain to appear in LIGO's band, and no gravitational wave has yet to be found in the S5 data. A second generation of LIGO detectors, Advanced LIGO, has been designed to be at least an order of magnitude more sensitive at several hundred Hz and above and include an impressive increase in bandwidth down to 10 Hz, dramatically increasing the chances of detection. To test some of Advanced LIGO's new technologies, an incremental upgrade to the detectors was carried out after S5 [8]. This project, Enhanced LIGO, culminated with the S6 science run from July 2009 to October 2010. Currently, construction of Advanced LIGO is underway. VIRGO and GEO will both undergo their own upgrades as well [6] [9]. See Figure 2-1 for achieved and theoretical noise curves.

The baseline Advanced LIGO design [10] improves upon Initial LIGO by featuring better seismic isolation, the addition of a signal extraction mirror at the output port, homodyne readout, and an increase in laser power from 10 W to 200 W. The substantial increase in laser power improves the shot-noise-limited sensitivity, but introduces a host of radiation pressure and thermally induced side effects that must be addressed for proper operation.

The recently completed Enhanced LIGO tested portions of the Advanced LIGO designs so unforeseen difficulties could be addressed and so that a more sensitive data taking run could take place. An output mode cleaner was designed, built and installed, and DC readout of the GW signal was implemented [11]. An Advanced LIGO active seismic isolation table was also built, installed, and tested [12]. In addition, the 10 W Initial LIGO laser was replaced with a 35 W laser [13]. Accompanying the increase in laser power, both the Alignment Sensing and Control and Input Optics were modified. The upgrades of these two subsystems make up the content of this dissertation.

CHAPTER 3 LASER INTERFEROMETERS FOR GRAVITATIONAL-WAVE DETECTION

3.1 Signal versus noise

The factors that must be considered in the design of any detector can be grouped into two categories: signal and noise. The ability to make a claim of detection is largely dependent on the magnitude of the signal to noise ratio (SNR). An SNR of 8 is desired for detection confidence in LIGO. For laser interferometers, the strength of the GW signal is proportional to the length of the arms and the amount of power in the arms. (See Eq. ??.) The change in the distance between the mirrors, ΔL , is bigger for a given strain the longer the arms. And with more circulating power, the greater the amount of power that will show up at the AS port for a given displacement from the dark fringe. Therefore, the two fundamental ways to make a GW produce a bigger signal in an interferometer are: 1) make the arms longer, and 2) increase the circulating power.

No matter how large a signal one might have, it won't be found confidently, or at all, if there is too much noise. The noise itself is best grouped into categories of displacement noise and sensing noise, which affect the length of the arms and the measurement of the signal, respectively. Interferometers for GW detection are plagued primarily by displacement noise below 70 Hz and sensing noise above 200 Hz.

In the next sections I will describe briefly the specific types of displacement and sensing noises affecting the sensitivity of laser interferometers. A summary of the noise budget is shown in Fig. ??.

3.1.1 Displacement noise

ground motion, thermal noise

seismic noise physically displaces the mirrors, resulting in changes in the length of the arm.

3.1.2 Sensing noise

stray light, shot noise

Shot noise is a quantum mechanical effect of the detection of photons which creates uncertainty in the phase of the light, and therefore the power, at the AS port.

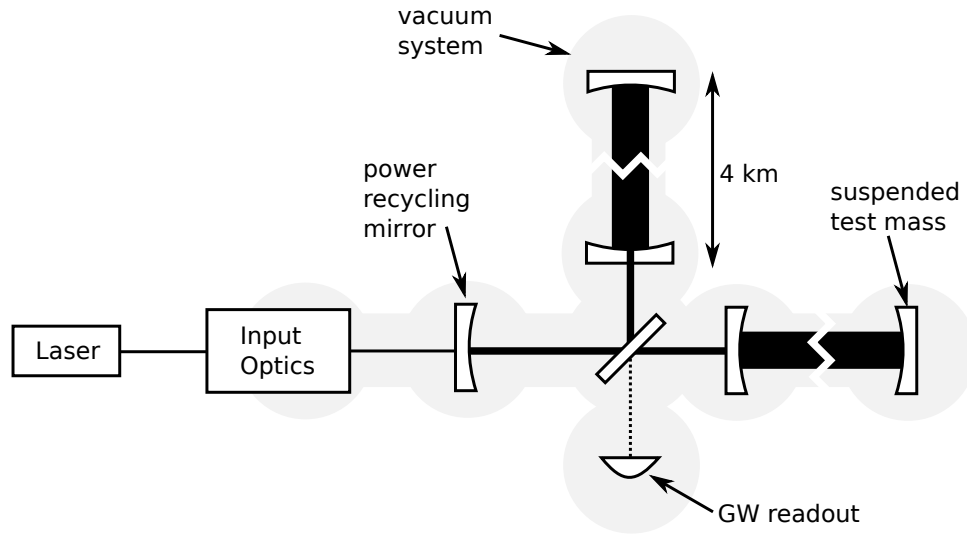


Figure 3-1. Power-recycled Fabry-Perot Michelson laser interferometer.

3.2 Power-recycled Fabry-Perot Michelson

The typical detector configuration is a power-recycled Fabry-Perot Michelson laser interferometer featuring suspended test masses in vacuum as depicted in Figure 3-1. A diode-pumped, power amplified, and intensity and frequency stabilized Nd:YAG laser emits light at 1064 nm. The laser is directed to a Michelson interferometer whose two arm lengths are set to maintain destructive interference of the recombined light at the anti-symmetric (AS) port. An appropriately polarized gravitational wave will differentially change the arm lengths, producing signal at the AS port proportional to the GW strain and the input power. The Fabry-Perot cavities in the Michelson arms and a power recycling mirror (RM) at the symmetric port are two modifications to the Michelson interferometer that increase the laser power in the arms and therefore improve the detector's sensitivity to GWs.

3.3 Measuring GW strain with light

3.3.1 Light as a photon

Consider two wave packets leaving the beam splitter of a Michelson interferometer at the same time, each heading down a different arm. If an appropriately polarized gravitational wave is

present, the amount of time the wave packet takes to travel down a stretched arm and back is:

$$t_{rt+} = \frac{2L}{c} \left(1 + \frac{h_+}{2} \right) \quad (3.3.1)$$

Likewise, for a compressed arm the roundtrip travel time is:

$$t_{rt-} = \frac{2L}{c} \left(1 - \frac{h_+}{2} \right) \quad (3.3.2)$$

There is a non-zero $2Lh_+/c$ difference in arrival times at the beam splitter, a quantity one could measure with an accurate stationary clock. This demonstrates intuitively that a laser interferometer can detect gravitational waves.

It should be noted that we had to use the approximation that the gravitational wave wavelength λ_{gw} is much larger than the interferometer arm length L . This means that the temporal variation of $h_+(t)$ is negligible during the time it takes the photon to make its roundtrip. Thus, h_+ is treated as a constant in Eqs. 3.3.1 and 3.3.2.

3.3.2 Light as a wave

The detector at the beam splitter is not a clock, but a photodetector which is sensitive to phase. It would be informative, therefore, to express the difference in arrival times as a difference in phase. To do so, we must move away from the photon model and think about the wave model of light. The light wave's phase is given by $\phi = \omega t$ where t is the proper time. Then, the difference in phase between the two light beams after each has completed its roundtrip is:

$$\Delta\phi = \phi_{rt+} - \phi_{rt-} = \frac{2L\omega}{c} h_+ \quad (3.3.3)$$

Two time derivatives yields

$$\frac{d^2\Delta\phi}{dt^2} = \frac{2L\omega}{c} \partial_t \partial_t h_+. \quad (3.3.4)$$

It can be shown [14] that the Riemann tensor in the TT gauge is $R_{tki} = -\frac{1}{2} \partial_t \partial_t h_{ki}$, and gauge invariant. Therefore, our physically measurable quantity can be expressed as being manifestly gauge invariant, proving that a laser interferometer can detect the effect of gravitational waves.

3.4 Power Recycled Michelson Interferometers

- phase detection, sidebands
- sub-systems, basic loops

3.5 More Laser Power

3.6 Digital Control in LIGO

The LIGO interferometers are interfaced through a digital control system.

CHAPTER 4 ANGULAR MIRROR MOTION

4.1 Introduction

For the interferometer to first achieve lock and then remain at its linear operating point, the mirrors need to point at one another and remain stationary with respect to this pointing. In practice, however, the mirrors move around due to three torque inputs to each mirror: the suspension, the actuators, and radiation pressure. Each torque produces an angular displacement of the mirror as governed by the mirror's torque to angle transfer function and results in either a static or dynamic misalignment.

The dynamic misalignments arise from torque introduced through the suspension from ground motion and through the actuators from an unbalanced piston force. Both of these torques create an angular motion independent of the state of the mirror's pointing. Radiation pressure torque, however, stands apart; its effect depends on the pointing of the mirror. A consequence is that even when all of the mirrors are perfectly aligned at all frequencies, the simple existence of light in the interferometer makes the arm cavities statically unstable when high enough laser powers are used.

This chapter discusses the causes of mirror angular displacement and the effects of residual mirror motion on the interferometer. Background material is provided as necessary, such as the dynamics of torsion pendula, and the geometric eigenfunctions of linear cavities. In all, I hope to convince the reader of the need for an Angular Sensing and Control subsystem.

4.2 The mirrors as torsion pendula

The mirrors in LIGO are torsion pendula. They are suspended from a single [xx m diameter](#) wire that makes contact with the bottom of the barrel of the mirror as shown in Fig. [4-1](#). Stand-offs glued just below the mirror's center of mass on both sides of the barrel mark the final point of contact of the wire with the mirror, and both ends of the wire are clamped to the top of a suspension cage. The mirror is free to twist an angle θ about a horizontal axis passing through

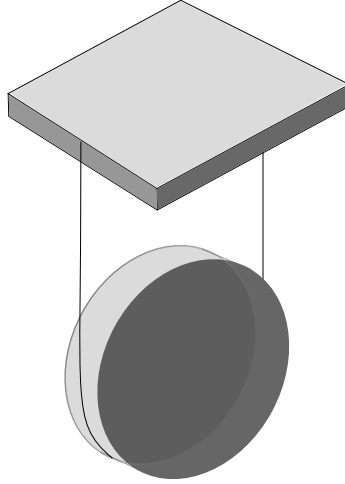


Figure 4-1. Cartoon of a LIGO suspension. [Improve this.](#)

its center of mass to create motion in *pitch* and about a vertical axis passing through its center of mass to create a motion in *yaw*.

The angular equation of motion of the mirror is governed by the sum of all torques on the mirror. First, let's consider the most simplistic scenario where there is only a pendulum restoring torque $\tau_p = -\kappa_p \theta$, where κ_p is the pendulum's torsional constant. The equation of motion is

$$I\ddot{\theta} + \kappa_p \theta = 0, \quad (4.2.1)$$

which has a solution of $\theta(t) = \sin(\omega_0 t)$, where $\omega_0 = \sqrt{\kappa_p/I}$ is the resonant angular frequency and I is the mirror's moment of inertia. The pendulum torsional constant serves to make the mirror oscillate indefinitely about its equilibrium position upon the slightest displacement.

4.2.1 Torque to angle transfer function

We are particularly interested in the pendulum's response to an external torque, such as seismic noise. In order to calculate the torque to angle transfer function, we must include an external torque term, τ_{ext} , in the equation of motion:

$$I\ddot{\theta} + \gamma\dot{\theta} + \kappa\theta = \tau_{ext}. \quad (4.2.2)$$

Here, we have also introduced a damping term, γ , to best model reality. Taking the Laplace transform to convert from the time domain to the frequency domain, we have:

$$Is^2\Theta + \gamma s\Theta + \kappa\Theta = \tau_{ext} \quad (4.2.3)$$

where s is a complex parameter. We are only interested in examining the transfer function for a pure sine wave excitation, $e^{i\omega t}$, so we substitute $s = i\omega$ to get

$$\text{TF} := \frac{\Theta}{\tau_{ext}} = \frac{1}{Is^2 + \gamma s + \kappa} = \frac{1/I}{\omega_0^2 - \omega^2 + i\gamma\omega/I} \quad (4.2.4)$$

which has poles at

$$s = s_{\pm} = \frac{-\gamma \pm \sqrt{\gamma^2 - 4I\kappa}}{2I}. \quad (4.2.5)$$

The resonant frequency of this system can be computed by finding the ω at which the amplitude of the transfer function, $[I^2[\omega^2 - \omega_0^2]^2 + \gamma^2\omega^2]^{-1/2}$, is maximized:

$$\omega_{res} = \sqrt{\omega_0^2 - \frac{\gamma^2}{2I^2}}. \quad (4.2.6)$$

We see that damping serves to reduce the resonant frequency.

A quantity used more often than γ for describing the losses of a system with a real resonance is the quality factor, $Q := \omega_{res}/\text{FWHM}$, where FWHM is that computed for the amplitude squared of the transfer function. When the losses are small, $\omega_{res} \approx \omega_0$ and $\text{FWHM} \approx \gamma/I$ (see Feynman 23-4). The quality factor is then well approximated by $Q = \sqrt{\kappa I}/\gamma$. The transfer function written in terms of Q is

$$\text{TF} = \frac{1/I}{\omega_0^2 - \omega^2 + i\omega\omega_0/Q}. \quad (4.2.7)$$

Figure 4-2 shows this torque to angle transfer function (for pitch) using the parameters of a LIGO core optic. For external torques applied to the mirror above its resonant frequency, the mirror acts like a free mass, one that is not held in place by suspension wires nor subject to damping. For torques applied to the mirror below its resonant frequency, the mirror's angle is determined by the inverse of the torsional constant.

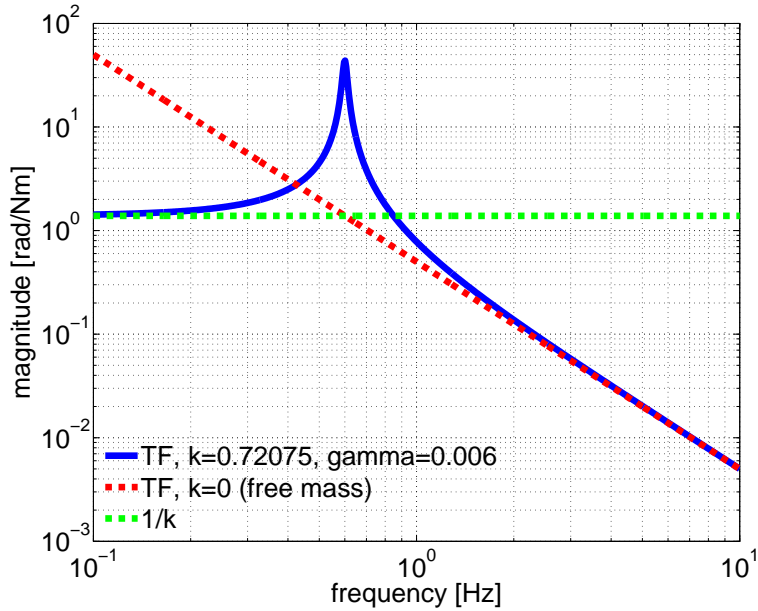


Figure 4-2. Torque to pitch transfer function of a LIGO core optic (blue). The optic acts like a free mass at high frequencies (green) and the DC magnitude of the transfer function is determined by the inverse torsional constant (red). A damping constant $\gamma = 0.006$ ($Q = 32$) was selected for pictorial reasons only. The resonant frequency of LIGO core optics in yaw is 0.5 Hz.

4.3 Seismic noise torque

Ground motion couples through both the seismic isolation table and the suspension. The torque it induces on the mirror creates pitch or yaw motion according to the torque to angle transfer function, Eq. 4.2.7. An example of the motion of the core test masses during a time of relatively quiet seismic noise at LLO is shown in Fig. 4-3.

At all times, whether the interferometer is locked or not, all suspended optics are velocity damped by the OSEM actuators. In addition, the 6 core optics are velocity damped by optical levers as well. The spectra in the figure are taken in the presence of this AC damping—it is, after all, the motion that will need to be controlled interferometrically.

4.4 Actuation noise torque

Length control couples to angle when the two are not perfectly diagonalized. Each mirror is equipped with four optical sensor and electro-magnetic (OSEM) actuators for providing control

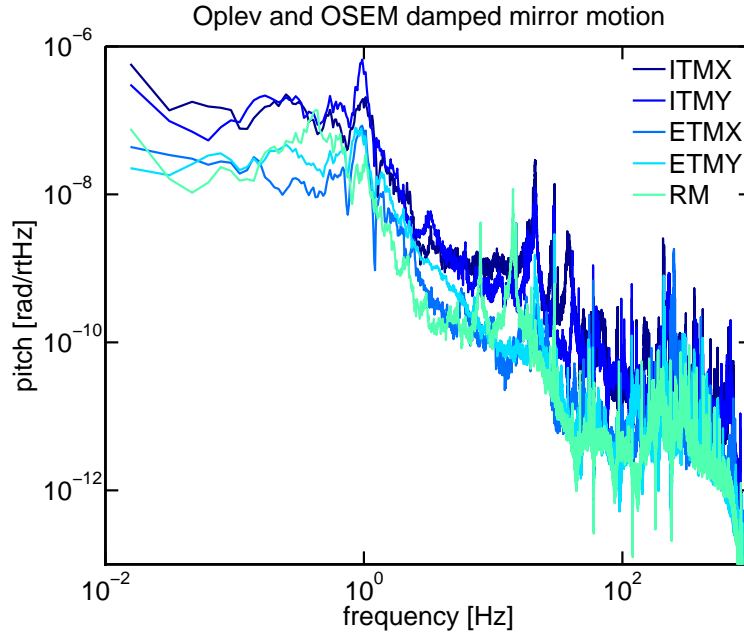


Figure 4-3. Typical angular motion of the core suspended mirrors in the absence of interferometric control. Velocity damping provided by the OSEMs and the optical levers is present. Above about 30 Hz, the plot does not represent real motion; the spectrum is limited by sensor (optical lever) noise. [Show the quadrature sum of angular motion due to the three sources discussed in this section.](#)

Figure 4-4. Angular motion induced by a 1% coupling of length actuation to angle.

to the mirror. Magnets arranged to form the four corners of a square are glued on the mirror's back surface, and the OSEM units envelop them. Length control of the cavities sends current of the same magnitude through each coil on a given mirror to provide a piston force for changing the mirror's position. However, small imbalances in inductor and magnetic strength result in a torque actuation in addition to a position actuation. This length to angle coupling, α , is on the order of 1%.

A typical length control signal provides a force with such and such a spectrum in units of m/rHz, which means the angular motion induced by L2A is as shown in Fig. ??.

4.5 Radiation pressure torque

Radiation pressure creates a torque when the beam impinges the mirror off-center. The force on the mirror due to radiation pressure is derived from the change in momentum of a photon

upon reflection off the mirror and results in:

$$F_{rp} = \frac{2P}{c}. \quad (4.5.1)$$

P is the power of the light reflected by the mirror and c is the speed of light. Assuming the beam of photons strikes the mirror perpendicular to its surface, the torque exerted on a mirror due to radiation pressure is

$$\tau_{rp} = \frac{2Px}{c} \quad (4.5.2)$$

where x is the distance of the beam from the mirror's center of mass.

For LIGO we must consider the effect of τ_{rp} on mirrors that form a linear cavity. As we show in the following subsection, the beam positions are coupled and dependent on the angles of the mirrors. The radiation pressure torques are likewise coupled to both mirrors. They create two orthogonal and power-dependent opto-mechanical modes through modification of the pendulum torque to angle transfer function, Eq. 4.2.7. In all, radiation pressure shapes the angular dynamics of the mirrors in LIGO and plays an important role in the design of an angular control system.

4.5.1 Tilt eigenmodes of a Fabry-Perot cavity

For a Fabry-Perot cavity as is used in the arms of the LIGO interferometer, the positions of the beams on the mirrors x_i are dependent on the angles of the mirrors θ_i according to the cavity's geometry:

$$\begin{bmatrix} x_1 \\ x_2 \end{bmatrix} = \frac{L}{1 - g_1 g_2} \begin{bmatrix} g_2 & 1 \\ 1 & g_1 \end{bmatrix} \begin{bmatrix} \theta_1 \\ \theta_2 \end{bmatrix}. \quad (4.5.3)$$

The g-factor is defined as $g_i = 1 - R_i/L$ where R is the radius of curvature of the mirror and L is the length of the cavity.

It is informative to diagonalize this matrix, $\mathbf{A} = \begin{bmatrix} g_2 & 1 \\ 1 & g_1 \end{bmatrix}$, and see what sets of mirror tilts and beam positions are independent from one another. Its eigenvalues are

$$\lambda_1 = \frac{g_1 + g_2 + \sqrt{(g_1 - g_2)^2 + 4}}{2} \quad (4.5.4)$$

$$\lambda_2 = \frac{g_1 + g_2 - \sqrt{(g_1 - g_2)^2 + 4}}{2} \quad (4.5.5)$$

and its eigenvectors are

$$\vec{v}_1 = \begin{bmatrix} 1 \\ \frac{g_1 - g_2 + \sqrt{(g_1 - g_2)^2 + 4}}{2} \end{bmatrix} \quad (4.5.6)$$

$$\vec{v}_2 = \begin{bmatrix} \frac{-g_1 + g_2 - \sqrt{(g_1 - g_2)^2 + 4}}{2} \\ 1 \end{bmatrix}. \quad (4.5.7)$$

Therefore, the matrix

$$\mathbf{P} = \begin{bmatrix} \vec{v}_1 & \vec{v}_2 \end{bmatrix} = \begin{bmatrix} 1 & \frac{-g_1 + g_2 - \sqrt{(g_1 - g_2)^2 + 4}}{2} \\ \frac{g_1 - g_2 + \sqrt{(g_1 - g_2)^2 + 4}}{2} & 1 \end{bmatrix} \quad (4.5.8)$$

diagonalizes \mathbf{A} such that

$$\mathbf{P}^{-1}\mathbf{A}\mathbf{P} = \begin{bmatrix} \lambda_1 & 0 \\ 0 & \lambda_2 \end{bmatrix} = \begin{bmatrix} \frac{g_1 + g_2 + \sqrt{(g_1 - g_2)^2 + 4}}{2} & 0 \\ 0 & \frac{g_1 + g_2 - \sqrt{(g_1 - g_2)^2 + 4}}{2} \end{bmatrix}. \quad (4.5.9)$$

These eigenvectors \vec{v}_1 and \vec{v}_2 form the orthogonal bases of mirror tilts in which we will describe each of the arm cavities for the remainder of this dissertation. In particular, since $\mathbf{A}\vec{v} = \lambda\vec{v}$, the beam displacements are proportional to the mirror tilts when the tilts are described by one of these two eigenvectors. Figure 4-5 illustrates a cavity in each of these two *eigenmodes* when using the LIGO cavity parameters as outlined in Table 4-1. The derivation of the dependence of cavity displacement a and cavity tilt α on mirror angles is in Appendix xx.

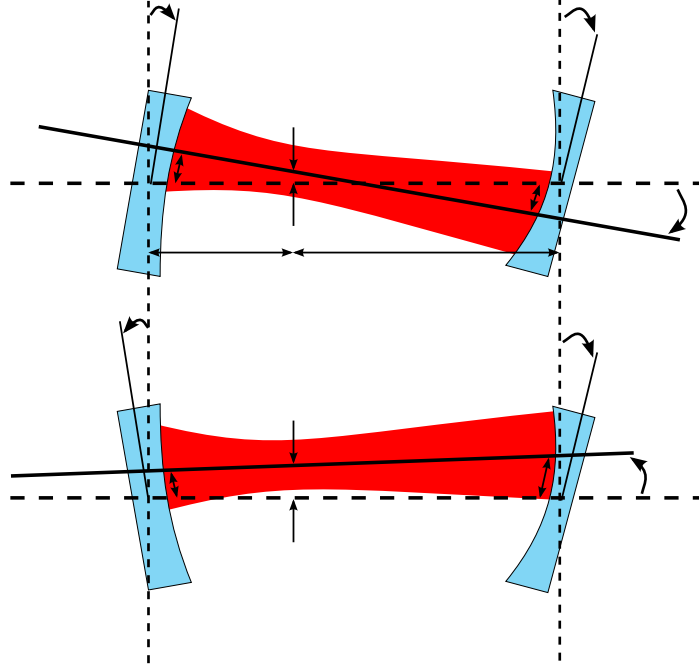


Figure 4-5. Illustration of the orthogonal modes of cavity tilt. The upper diagram shows tilts given by eigenvector \vec{v}_2 and the lower diagram shows \vec{v}_1 .

Table 4-1. Geometric parameters of the LIGO arm cavity eigenmodes. x_i are the beam locations on the mirrors relative to center, a is the cavity axis displacement at the waist, and α is the cavity axis angle with respect to a line joining the centers of the mirrors. Differences between LLO and LHO arise from the mirrors having different radii of curvature at the two sites.

cavity parameter	LLO \vec{v}_1 mode	LLO \vec{v}_2 mode	LHO \vec{v}_1 mode	LHO \vec{v}_2 mode
$ x_1 $ [mm/urad]	9.88	2.44	8.20	2.51
$ x_2 $ [mm/urad]	10.84	2.22	9.35	2.20
$ a $ [mm/urad]	10.17	1.01	8.48	1.34
$ \alpha $ [urad/urad]	0.24	1.17	0.29	1.18

4.5.2 Soft and hard modes

We have seen that mirror torques due to radiation pressure are a function of beam positions (Eq. 4.5.2) and that beam positions are a function of mirror angles (Eq. 4.5.3). We are now ready to combine these two observations to define radiation pressure torque as a function of mirror

angle:

$$\begin{bmatrix} \tau_{rp,1} \\ \tau_{rp,2} \end{bmatrix} = \frac{2PL}{c(1-g_1g_2)} \begin{bmatrix} g_2 & 1 \\ 1 & g_1 \end{bmatrix} \begin{bmatrix} \theta_1 \\ \theta_2 \end{bmatrix}. \quad (4.5.10)$$

This is more succinctly expressed as

$$\vec{\tau}_{rp} = -\mathbf{K}_{rp}\vec{\theta}, \quad (4.5.11)$$

where \mathbf{K}_{rp} is called the *torsional stiffness matrix*.

We arrive at the purpose of this section—to evaluate how radiation pressure affects the suspended mirror’s motion. In order to examine its effect, we will work in the basis of the diagonalized \mathbf{K}_{rp} , using the eigenvectors \vec{v}_1 and \vec{v}_2 as two different cases of mirror tilts. The total torque on each mirror for each of these two cases ($i = 1, 2$) is the sum of the restoring torque of the pendulum and the radiation pressure torque:

$$\vec{\tau}_{tot_i} = \vec{\tau}_{rp} + \vec{\tau}_p = -[\kappa_{rp_i} + \kappa_p]\vec{v}_i \quad (4.5.12)$$

$$= -\left[-\frac{2PL}{c(1-g_1g_2)}\lambda_i + \kappa_p\right]\vec{v}_i \quad (4.5.13)$$

$$:= -\kappa_{tot_i}\vec{v}_i \quad (4.5.14)$$

with λ_i and \vec{v}_i defined by Eqs. (4.5.5) and (4.5.7).

Here we make an observation of great significance for the rest of the paper. While the new torsional constant, κ_{tot_i} , is positive, the torque is restorative and the mirror will return to its equilibrium position. However, as soon as κ_{tot_i} becomes negative, the system is unstable as the mirror will be pushed yet further away from equilibrium. And of course, when $\kappa_{tot_i} = 0$, $\tau_{tot_i} = 0$. Explicitly, our stability criteria are

$$\text{stable: } \frac{2PL\lambda_i}{c(1-g_1g_2)} < \kappa_p \quad (4.5.15)$$

$$\text{unstable: } \frac{2PL\lambda_i}{c(1-g_1g_2)} > \kappa_p. \quad (4.5.16)$$

We now turn to examine this stability criteria for the specific case of LIGO’s arm cavities. First, in order for a Gaussian beam to fit properly between two mirrors and thus form a resonant

Table 4-2. Torsional constants (pitch) for the soft and hard modes of a typical Initial LIGO power and the highest of Enhanced LIGO powers. The soft mode in Enhanced LIGO is unstable.

	P_{circ} (kW)	κ_p (Nm/rad)	$\kappa_{tot1}, \text{ soft}$ (Nm/rad)	$\kappa_{tot2}, \text{ hard}$ (Nm/rad)
iLIGO	9	0.721	0.0734	0.867
eLIGO	40	0.721	-2.18	1.38

cavity, the g-factors are restricted to $0 < g_1 g_2 < 1$. Therefore, the sign of the left-hand side of Eq. 4.5.16 is determined solely by that of λ , and it can be shown from the g-parameter restriction that λ_1 is always positive and λ_2 is always negative. Since $\kappa_p > 0$, the mode described by \vec{v}_1 will be either stable or unstable, and the mode described by \vec{v}_2 will always be stable. Namely, as power P increases, κ_{tot1} decreases, creating a softer spring, but κ_{tot2} increases, creating a stiffer spring. Thus arise the terms *soft* and *hard* to describe the two eigenmodes.

To see how radiation pressure modifies the torque to angle transfer function of the pendula, κ_{tot} is used in Eq. 4.2.7 instead of just κ_p . The effect is that ω_0 is now not only a function of κ_p , but also of κ_{rp} :

$$\text{soft : } \omega_0 = \sqrt{\frac{-\frac{2PL}{c(1-g_1g_2)} \frac{g_1+g_2+\sqrt{(g_1-g_2)^2+4}}{2} + \kappa_p}{I}} \quad (4.5.17)$$

$$\text{hard : } \omega_0 = \sqrt{\frac{-\frac{2PL}{c(1-g_1g_2)} \frac{g_1+g_2-\sqrt{(g_1-g_2)^2+4}}{2} + \kappa_p}{I}} \quad (4.5.18)$$

Figure 4-6 shows κ_{tot_i} for a LIGO arm cavity as a function of circulating power and Table 4-2 highlights the specific numbers for Initial and Enhanced LIGO powers. The corresponding hard and soft transfer functions are plotted in Fig. 4-7.

4.5.3 Stability

Let's re-examine the stability criteria, but from the transfer function perspective. The poles s_{\pm} of the transfer function indicate whether a system will respond to an excitation in a sinusoidal and/or exponential manner since the inverse Laplace transform of the transfer function is the impulse response. As long as the poles are negative real or imaginary, the angular motion will

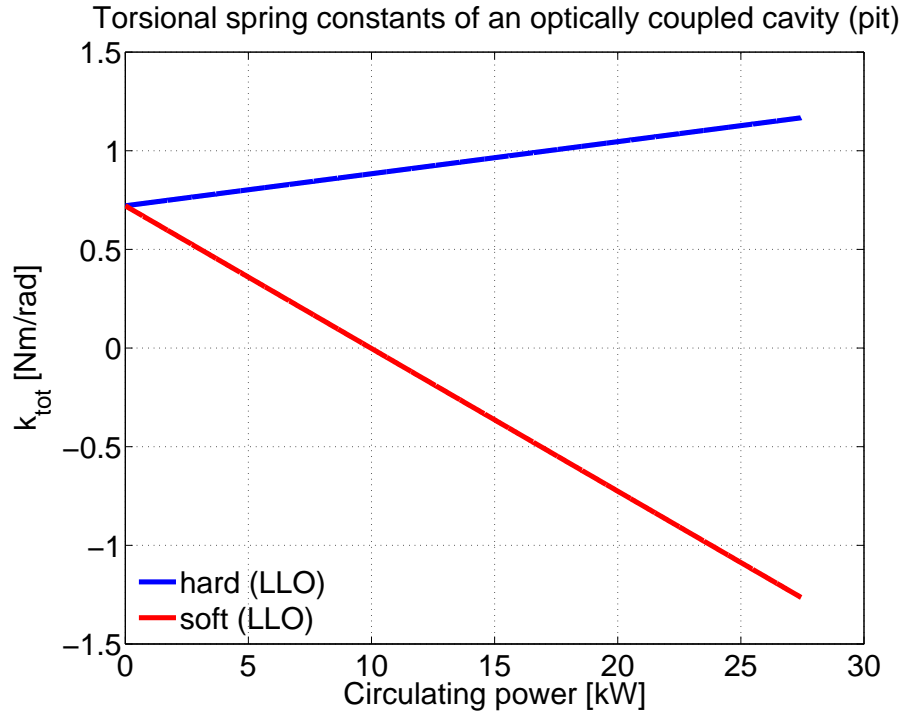


Figure 4-6. Torsional spring constants (pitch) of an optically coupled cavity for LLO parameters. The soft mode is unstable when the spring constant is negative.

Table 4-3. Conditions on torsional constant κ for determining system stability.

κ condition	pole s_+	impulse response
$\kappa < 0$	real positive	statically unstable
$\kappa = 0$	zero	
$0 < \kappa < \gamma^2/4I$	real negative	stable decay
$\kappa > \gamma^2/4I$	real negative, and imaginary	stable, oscillatory

decay or be sinusoidal. However, if a pole is in the right half of the s -plane, the system's motion will experience exponential growth.

Referring to the equation for the poles, Eq. 4.2.5, we can make a table of conditions on κ for s_{\pm} to be in a particular half of the s -plane. First, we notice that s_- will always be in the left half of the plane or along the imaginary axis and that s_+ is the potentially problematic pole. All possibilities for the pole in question are enumerated in Table 4-3 and demonstrate that as is shown in the previous subsection, stability is determined by the sign of κ . Figure 4-8 shows how the pole location changes as a function of κ .

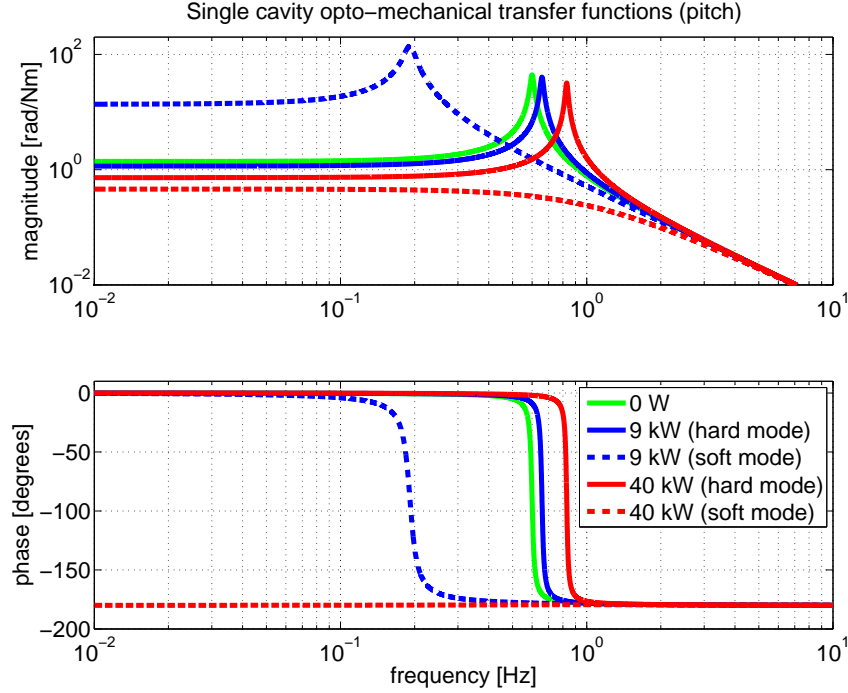


Figure 4-7. Single cavity opto-mechanical transfer function for pitch. The resonant frequency increases with power for the hard mode, but decreases for the soft mode, eventually becoming imaginary. $P_{circ} = 9$ kW (5.25 W input) was a typical operating power for Initial LIGO and $P_{circ} = 40$ kW (23.5 W input) is the highest of powers reached for Enhanced LIGO.

4.6 How much suppression is necessary?

The requirements for the amount of angular suppression arise from the effect of residual angular motion on the interferometer. Power fluctuations in the interferometer, for example, put sidebands on all lines in the DARM spectra at the frequency of the fluctuations, creating broadband up-conversion. Misalignment can create a contrast defect, a difference in the amount of power in one arm compared to the other.

4.7 Appendix xx–misaligned cavity axis

Here I provide the geometric argument that shows how to calculate the tilt a and displacement α of a cavity as a function of mirror misalignment. Cavity tilt is defined by the angle formed between the line that connects the two beam spots (as given by Eq. 4.5.3) and the line joining the centers of the mirrors. Cavity displacement uses the same two lines, yet is defined

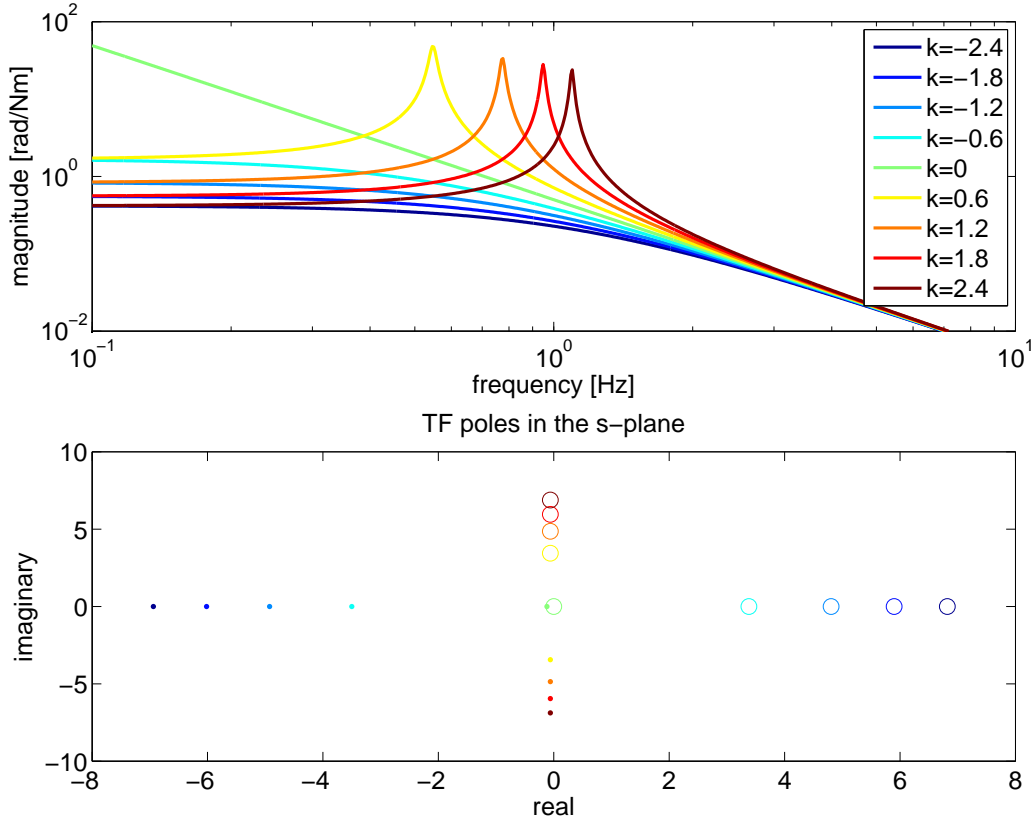


Figure 4-8. Torque to pitch transfer function (upper plot) and poles (lower plot) as a function of torsional constant for a fixed damping coefficient of $\gamma^2/4I = 1.77 \times 10^{-4}$. Circles show s_+ and dots show s_- . Poles in the right half of the s-plane indicate the system is unstable. This range of κ represents the torsional constants experienced while powering up Enhanced LIGO.

by the distance between them at the location of the waist of the resonant spatial mode. Based on pure geometry, the cavity displacement and tilt are:

$$\begin{bmatrix} a \\ \alpha \end{bmatrix} = \frac{1}{L} \begin{bmatrix} z_2 & z_1 \\ -1 & 1 \end{bmatrix} \begin{bmatrix} x_1 \\ x_2 \end{bmatrix} \quad (4.7.1)$$

where z_i is the distance to the waist from mirror i calculated as:

$$z_1 = \frac{g_2(1 - g_1)L}{g_1 + g_2 - 2g_1g_2} \quad (4.7.2)$$

$$z_2 = L - z_1. \quad (4.7.3)$$

Clearly, we can combine Eqs. (4.5.3) and (4.7.1) to arrive at an equation directly relating mirror tilt to cavity displacement and tilt:

$$\begin{bmatrix} a \\ \alpha \end{bmatrix} = \frac{1}{1 - g_1g_2} \begin{bmatrix} g_2z_2 + z_1 & z_2 + g_1z_1 \\ -g_2 + 1 & -1 + g_2 \end{bmatrix} \begin{bmatrix} \theta_1 \\ \theta_2 \end{bmatrix}. \quad (4.7.4)$$

CHAPTER 5

SENSING AND CONTROLLING MIRROR MOTION IN THE RADIATION PRESSURE EIGENBASIS

5.1 Introduction

In this chapter I show how the angular displacements are sensed and why control filters implemented in the eigenbasis of radiation pressure torques is best.

5.2 Sensing

There are five main subsets of sensor systems for the ASC:

- OSEMs
- optical levers (MMT3, RM, BS, ITMX, ITMY, ETMX, ETMY)
- camera image (BS)
- quadrant photodiodes (QPD_X, QPD_Y)
- wavefront sensors (WFS₁, WFS₂, WFS₃, WFS₄)

Together, these sensors need to provide enough information to derive adequate control signals for 9 mirrors in both pitch and yaw. Both absolute motion (AC) and relative motion (DC) need to be suppressed. The OSEMs and optical levers provide local AC control to the mirrors. The video camera and the QPDs control the pointing of the input beam; the video camera works at DC and the QPDs at both DC and AC. The WFS provide the top level fine tuning of DC and AC control to the 5 main mirrors.

5.2.1 OSEMs

The most basic level of control is local damping of each suspended optic provided by the OSEMs. This is always on, even when the interferometer loses lock. It works by sending current through the OSEM coils to keep a constant amount of light on the OSEM shadow sensor.

5.2.2 Optical levers

The optical levers are local to each large optic and provide a record at all times of pitch and yaw pointing of each mirror with respect to the ground. The mirrors are velocity-damped only by the optical levers; they are not controlled at DC. The optical lever is a HeNe laser beam that reflects off of the mirror and onto a QPD. Both the laser and QPD are mounted on heavy piers to

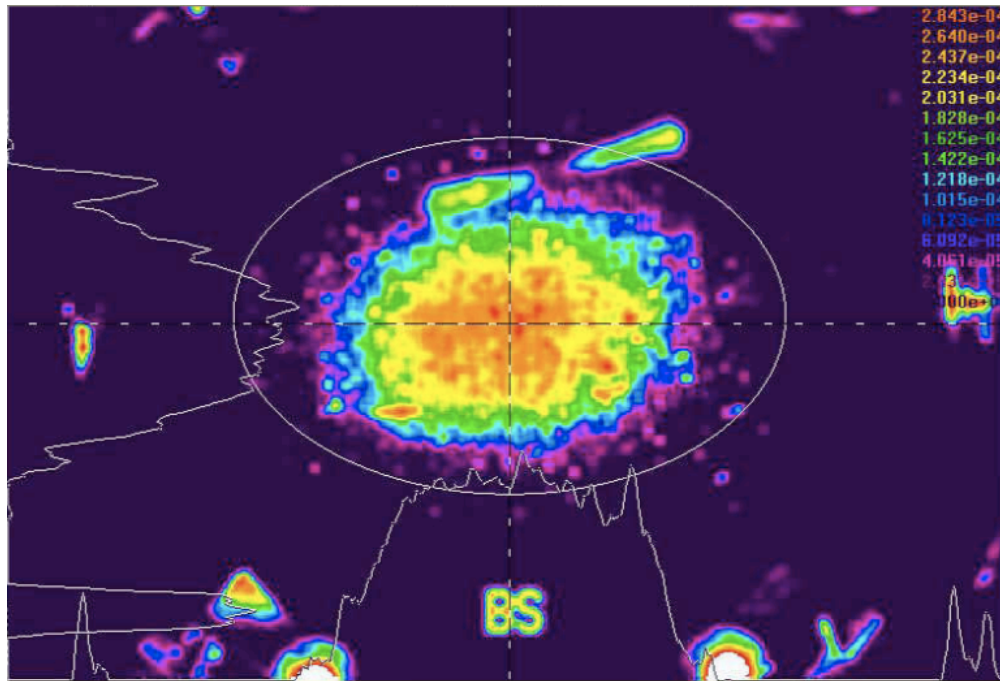


Figure 5-1. Image of beam on beam splitter as used for the beam centering servo.

reduce the seismic noise contribution to the QPD signal. The optical lever provides a feedback signal to the mirror's coils to reduce the sensed motion. Each large optic has its own independent optical lever loop which is almost always on, even when the interferometer is out of lock. The optical lever loops provide the second level of controlled stabilization of the mirrors, after only the local damping.

5.2.3 Camera image

The most primitive sensor is that of the physical video camera. The video camera monitors the location of the spot on the beam splitter, thus serving as a sensor of the pointing of the input beam. The image of the speckle of light reflected off of the beam splitter (see Fig. 5-1) is fed into a labview program which integrates the intensity of the image to identify the coordinates of the center of the beam spot. This is compared with a hardcoded desired center location and a mirror upstream, MMT1 is moved to redirect the input beam, minimizing the difference between the desired and actual beam spot location on the BS.

5.2.4 QPDs

QPD_X and QPD_Y see the small amount of light that is transmitted through the ETMs, providing a monitor of the modal axes of the arm cavities. Together with the , they maintain the alignment of the input . QPD_X

5.2.5 WFSs

The wavefront sensors provide the most sophisticated form of measuring angular motion of the mirrors. Their frame of reference is the fundamental Gaussian mode of the interferometer cavities (x-arm, y-arm, recycling cavity) as aligned to ????. All of the mirrors globally follow the pointing of the input beam (via the QPDs) which is in turn stabilized to the center of the beam splitter (via the BCS) at frequencies well below the pendulum resonances. The job of the wavefront sensors is to keep the mirrors aligned to one another up to several Hz within this hierarchy of alignment. The WFS provide DC and AC control to the mirror angles.

5.3 Control

When the gain is really high, comparing the calibrated error and control signals shows just what the control loop is doing. The error is the residual and the control is what there would be without the loop.

$\text{error} * (1+G)$ is the motion without the loop, where G is the open loop gain.

- optical lever calibration
- residuals, perhaps for different kinds of seismic
- compare to mirror motion with no ifo (demonstrate ASC suppression)

5.4 Sensor noise and noise contribution to DARM

5.5 Solving the noise problem with the eigenbasis

5.6 ASC to DARM noisebudget

The cut-off frequency of the lowpass filters for the WFS control are of particular importance in the DARM noisebudget. The lowpass filter is necessary for suppressing the impression of sensing noise on suspension control.

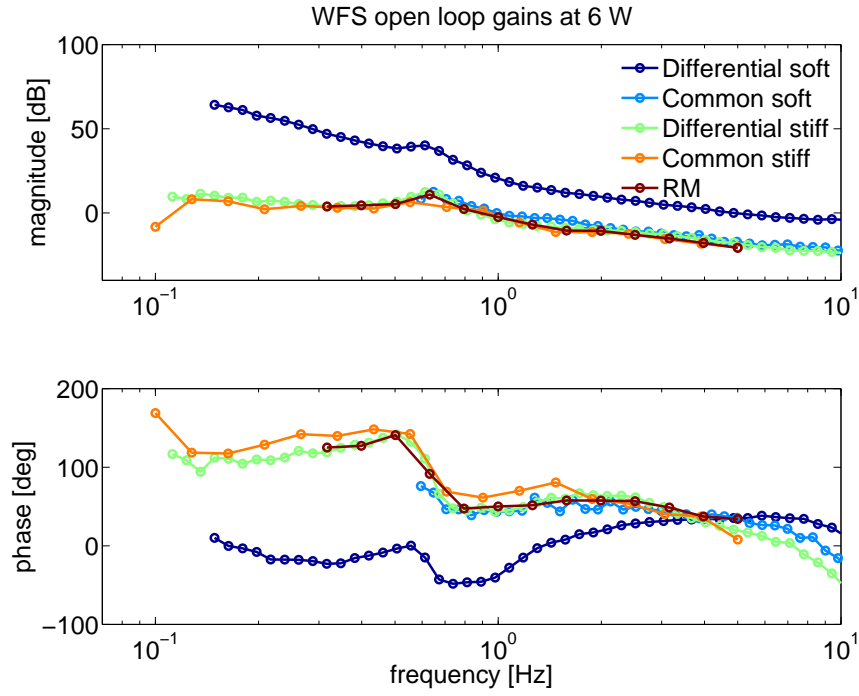


Figure 5-2. Pitch open loop gains of the 5 WFS loops as measured with 6 W input power.

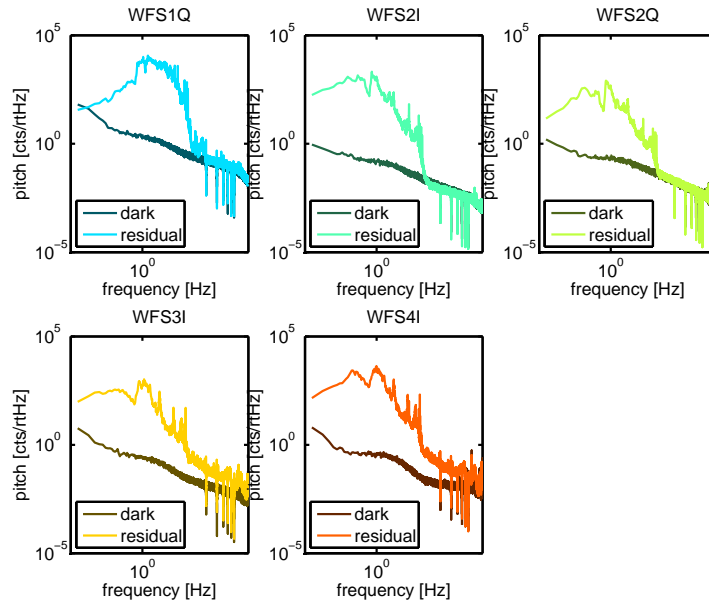


Figure 5-3. WFS sensor noise budget.

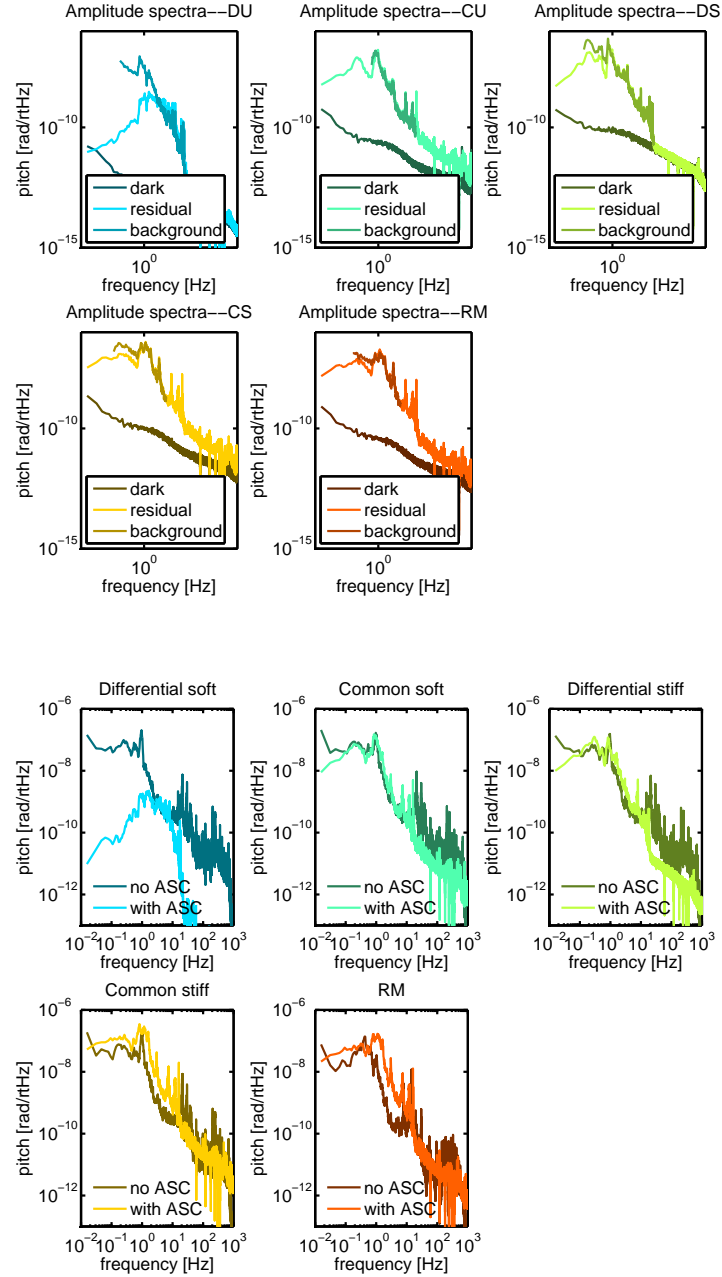


Figure 5-4. Top: Comparison of motion with and without the ASC. Eigenbasis residual during 10 W lock, and background derived from loop correction. Completely different day from bottom plot. Bottom: Propagation of sensor signals from 10 W lock through input matrix and power scaling to eigenbasis, compared with eigenbasis reconstruction of optical lever signals when interferometer not locked, but optics under oplev damping. Data are taken 45 minutes apart.

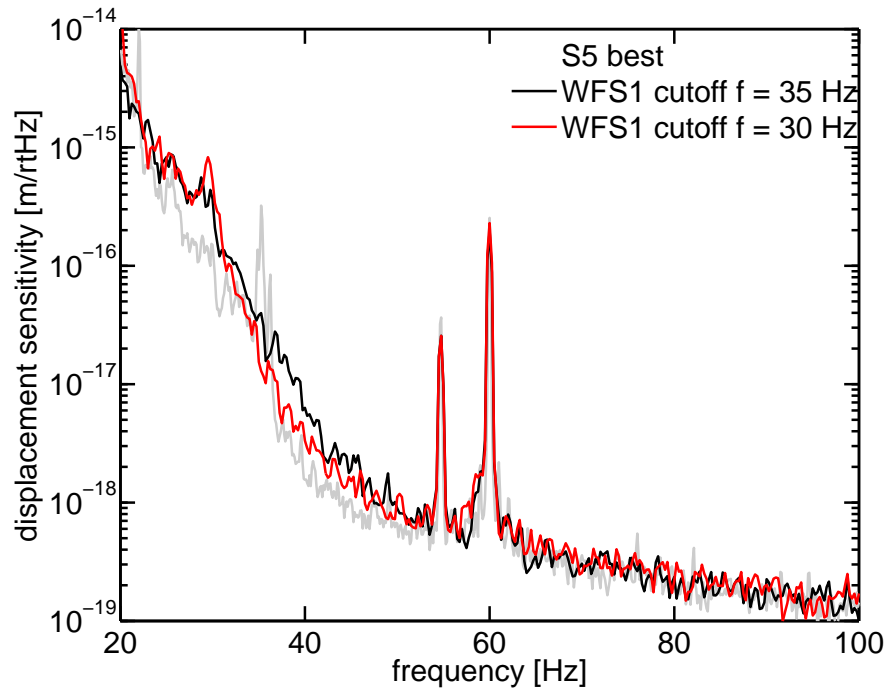


Figure 5-5. Effect of the WFS1 lowpass filter cutoff frequency on strain sensitivity.

5.7 Beam spot motion

- calibration
- residuals, perhaps for different kinds of seismic

5.8 Heating related measurements

- effect of PRC g-parameter on ASC sensing matrix
- SPOB power scaling

5.9 DC readout related measurements

- RF created from DC offset beam moving on WFS1
- RF vs DC vs power comparison of (AS) beam spot motion on WFS1

5.10 ASC noisebudget

- seismic - breakdown of source of motion
- L2A

- input beam
- electronics noise
- shot noise

CHAPTER 6
EXPERIMENTAL MEASUREMENT OF THE SIDLES-SIGG EFFECT

6.1 Measured modes

CHAPTER 7

SUMMARY



Figure 7-1. Reflected beam from the Advanced LIGO pre-mode cleaner.

REFERENCES

- [1] J. Sidles and D. Sigg, Physics Letters A **354**, 167 (2006), ISSN 03759601, URL <http://dx.doi.org/10.1016/j.physleta.2006.01.051>.
- [2] E. Hirose, K. Kawabe, D. Sigg, R. Adhikari, and P. R. Saulson, Appl. Opt. **49**, 3474 (2010), URL <http://dx.doi.org/10.1364/AO.49.003474>.
- [3] L. Barsotti and M. Evans, Tech. Rep. T080186, LIGO Laboratory (2009).
- [4] P. Linsay, P. Saulson, R. Weiss, and S. Whitcomb, Tech. Rep. T830001, Massachusetts Institute of Technology (1983).
- [5] B. P. Abbott, R. Abbott, R. Adhikari, P. Ajith, B. Allen, G. Allen, R. S. Amin, S. B. Anderson, W. G. Anderson, M. A. Arain, et al., Reports on Progress in Physics **72**, 076901+ (2009), ISSN 0034-4885, URL <http://dx.doi.org/10.1088/0034-4885/72/7/076901>.
- [6] F. Acernese, P. Amico, M. Alshourbagy, F. Antonucci, S. Aoudia, P. Astone, S. Avino, L. Baggio, G. Ballardin, F. Barone, et al., Journal of Optics A: Pure and Applied Optics **10**, 064009+ (2008), ISSN 1464-4258, URL <http://dx.doi.org/10.1088/1464-4258/10/6/064009>.
- [7] H. Lück, M. Hewitson, P. Ajith, B. Allen, P. Aufmuth, C. Aulbert, S. Babak, R. Balasubramanian, B. W. Barr, S. Berukoff, et al., Classical and Quantum Gravity **23**, S71 (2006), ISSN 0264-9381, URL <http://dx.doi.org/10.1088/0264-9381/23/8/S10>.
- [8] R. Adhikari, P. Fritschel, and S. Waldman, Tech. Rep. T060156, LIGO Laboratory (2006), URL <https://dcc.ligo.org/cgi-bin/DocDB/ShowDocument?docid=7384>.
- [9] H. Lück, C. Affeldt, J. Degallaix, A. Freise, H. Grote, M. Hewitson, S. Hild, J. Leong, M. Prijatelj, K. A. Strain, et al., Journal of Physics: Conference Series **228**, 012012+ (2010), ISSN 1742-6596, URL <http://dx.doi.org/10.1088/1742-6596/228/1/012012>.
- [10] Advanced LIGO Systems Group, Tech. Rep. T010075, LIGO Laboratory (2009), URL <https://dcc.ligo.org/cgi-bin/DocDB/ShowDocument?docid=5489>.
- [11] T. Fricke, N. Smith, R. Abbott, R. Adhikari, K. Dooley, M. Evans, P. Fritschel, V. Frolov, K. Kawabe, and S. Waldman, in preparation (2011), URL <https://dcc.ligo.org/cgi-bin/private/DocDB/ShowDocument?docid=8442>.
- [12] J. S. Kissel, Ph.D. thesis, Louisiana State University (2010).
- [13] M. Frede, B. Schulz, R. Wilhelm, P. Kwee, F. Seifert, B. Willke, and D. Kracht, Opt. Express **15**, 459 (2007), URL <http://dx.doi.org/10.1364/OE.15.000459>.
- [14] D. Garfinkle (2005), [gr-qc/0511083](https://arxiv.org/abs/gr-qc/0511083), URL <http://arxiv.org/abs/gr-qc/0511083>.

- [15] J. Camp, D. Reitze, and D. Tanner, Tech. Rep. T960170, LIGO Laboratory (1996), URL <https://dcc.ligo.org/cgi-bin/DocDB/ShowDocument?docid=28745>.
- [16] P. Fritschel, R. Bork, G. González, N. Mavalvala, D. Ouimette, H. Rong, D. Sigg, and M. Zucker, Appl. Opt. **40**, 4988 (2001), URL <http://dx.doi.org/10.1364/AO.40.004988>.
- [17] *Electro-Optic Modulators and Modulation for Enhanced LIGO and Beyond* (Optical Society of America, 2008), URL <http://www.opticsinfobase.org/abstract.cfm?id=169025>.
- [18] M. Zucker, Tech. Rep. T020113, LIGO Laboratory (2002), URL <https://dcc.ligo.org/cgi-bin/DocDB/ShowDocument?docid=27031>.
- [19] E. Khazanov, N. F. Andreev, A. Mal'shakov, O. Palashov, A. K. Poteomkin, A. Sergeev, A. A. Shaykin, V. Zelenogorsky, I. A. Ivanov, R. Amin, et al., IEEE Journal of Quantum Electronics **40**, 1500 (2004), ISSN 0018-9197, URL <http://dx.doi.org/10.1109/JQE.2004.834766>.
- [20] T. Delker, R. Adhikari, S. Yoshida, and D. Reitze, Tech. Rep. T970143, LIGO Laboratory (1997), URL <https://dcc.ligo.org/cgi-bin/DocDB/ShowDocument?docid=28875>.
- [21] P. Kwee, F. Seifert, B. Willke, and K. Danzmann, The Review of scientific instruments **78** (2007), ISSN 0034-6748, URL <http://dx.doi.org/10.1063/1.2754400>.

BIOGRAPHICAL SKETCH

Kate's biography.